

From synthetic turbulence to true solutions: A deep diffusion model for discovering periodic orbits in the Navier-Stokes equations

Jeremy P. Parker^{1,*} and Tobias M. Schneider^{2,†}

¹*Division of Mathematics, University of Dundee, Dundee DD1 4HN, United Kingdom*

²*Emergent Complexity in Physical Systems Laboratory (ECPS),*

École Polytechnique Fédérale de Lausanne, 1015 Lausanne, Switzerland

(Dated: February 27, 2026)

Generative artificial intelligence has shown remarkable success in synthesizing data that mimic complex real-world systems, but its potential role in the discovery of mathematically meaningful structures in physical models remains underexplored. In this work, we demonstrate how a generative diffusion model can be used to uncover previously unknown solutions of a nonlinear partial differential equation: the two-dimensional Navier-Stokes equations in a turbulent regime. Trained on data from a direct numerical simulation of turbulence, the model learns to generate time series that resemble physically plausible trajectories. By carefully modifying the temporal structure of the model and enforcing the symmetries of the governing equations, we produce synthetic trajectories that are periodic in time, despite the fact that the training data did not contain periodic trajectories. These synthetic trajectories are then refined into true solutions using an iterative solver, yielding 111 new periodic orbits (POs) with very short periods. Our results reveal a previously unobserved richness in the PO structure of this system and suggest a broader role for generative AI: not as replacements for simulation and existing solvers, but as a complementary tool for navigating the complex solution spaces of nonlinear dynamical systems.

I. INTRODUCTION

The fluid dynamics of turbulence is the archetypal example of a high-dimensional chaotic system in which the governing equations are known perfectly, yet physically meaningful predictions and interpretations are inherently limited. Despite well-developed numerical methods for evolving flows from initial conditions, many basic questions about the geometry and structure of turbulent dynamics remain.

One promising line of investigation seeks to understand turbulent flows not in terms of statistical parameterizations or low-order approximations, but as a collection of exact solutions to the equations themselves – particularly periodic orbits (POs) and relative periodic orbits (RPOs), which recur in time either exactly or modulo a symmetry. These solutions are mathematically well-defined, physically interpretable, and in low-dimensional systems have been shown to form the organizing skeleton of chaotic dynamics [1, 2]. In a sense that can be made mathematically rigorous [3], all chaotic trajectories can be understood as a concatenation of very short periodic orbits. These shortest periodic orbits are the fundamental units of the dynamics, much like a Fourier basis in function space: multiple simple components combine to generate the rich complexity of chaotic trajectories.

While this periodic orbit theory is well-established for low-dimensional systems, its application to partial differential equations (PDEs) like the Navier-Stokes equations remains limited, in part because finding the relevant invariant solutions is difficult [4]. Traditional methods for PO discovery rely on either targeted continuation from known solutions or searches for close recurrences in a time series, both of which are computationally intensive and tend to find only a narrow subset of orbits. The challenge is not just solving the equations, but identifying where to look. Despite over a decade of study of the particular system we consider here – at exactly the same parameter value $Re = 40$ [5–9] – we still do not have a finite collection of the shortest periodic orbits, which should be the simplest possible decomposition of the dynamics, the ‘building blocks’ of turbulence.

Recent advances in machine learning, and in particular generative AI, have introduced powerful new tools for navigating high-dimensional data spaces. Diffusion models, now state-of-the-art in image and audio generation, are especially adept at sampling complex, high-dimensional distributions and producing outputs that are statistically plausible and qualitatively convincing. However, when applied to physical systems, the outputs they generate are not guaranteed a priori to satisfy the governing equations. Some previous studies have used machine learning techniques to generate guesses for POs [4, 10, 11]. These have focused on attempting to understand the system’s dynamics or the geometry of the state space, and still use somewhat crude methods for generating the ‘loops’ that geometrically

* jpark002@dundee.ac.uk

† tobias.schneider@epfl.ch

represent the guesses. Our intent is instead to directly generate state space loops that everywhere approximate the dynamics, and combine these with our existing parallel-in-time methods for converging periodic solutions [9].

Here we explore how generative models can be repurposed to aid in the discovery of ‘exact’ (up to machine precision) solutions in a chaotic PDE system. Our approach combines a diffusion model trained on a turbulent simulation of the two-dimensional Navier-Stokes equations with a massively parallel, GPU-accelerated Levenberg-Marquardt solver built on MINRES iterations. The model itself has no access to the dynamics: it is trained solely on time series of vorticity fields, without knowledge of the underlying equations or any notion of periodicity. In principle, the same method could be applied to any spatiotemporal dataset – for example, a video of clouds – and would learn only the statistical patterns in the data, not the rules that generated them.

After training, we modify the model architecture so that it produces periodic trajectories without retraining the weights. We use it to generate thousands of candidate orbits, which are then refined into exact solutions using our solver. Many of the resulting solutions are qualitatively different from the synthetic guesses they were seeded from, indicating that the generative model alone is insufficient. Nevertheless, the converged solutions retain many of the qualitative features of the synthetic trajectories. It is the combination of plausible and varied candidates with a robust convergence algorithm that makes the method effective: without the solver, the trajectories would remain approximate; without the model, we would lack the diversity of informed guesses needed to find new orbits.

A key feature of our method is that it respects the symmetries of the governing equations. We incorporate the known equivariance properties of the Navier-Stokes system into the model design to ensure that generated solutions preserve continuous and discrete spatial symmetries. A convolutional neural network – which automatically respects translation equivariances and can be carefully designed to encode discrete symmetries [12] – is a natural architecture to exploit these properties. This allows us to generate candidates that lie in specific symmetry subspaces, or that exhibit relative periodicity under symmetry transformations. Symmetry equivariant diffusion models are beginning to be used in other areas of the physical sciences [13–15]. It is important to emphasize that even though our model respects the symmetries of the governing equations, it knows nothing of the actual equations, contrary to so-called ‘physics-informed’ approaches [16–18].

More broadly, our work reflects the growing need for interpretability and physical validation in generative AI. While diffusion models are capable of producing high-quality synthetic data, the challenge in scientific applications is to connect those outputs back to true, physically meaningful structures. By combining generative sampling with strict validation against the governing equations, we show that such a connection is not only possible but fruitful. The result is a workflow in which AI augments, rather than replaces, classical numerical methods, helping to navigate the vast solution space of a complex system and to identify previously unknown invariant structures.

We apply this approach to the two-dimensional Kolmogorov flow at moderate Reynolds number ($Re = 40$), which has become the standard testbed for these approaches to turbulence. We train a diffusion model on vorticity time-series from a turbulent simulation (using segments that all contain a high-dissipation ‘bursting’ event), without providing the network with the equations or any notion of periodicity in time. After training, we modify the sampling procedure so that the model produces *periodic or relative-periodic* trajectories *without retraining the weights*. These synthetic loops are then converged with a massively parallel, GPU-accelerated Levenberg–Marquardt method implemented via MINRES iterations [9]. Using this workflow, we obtain *111 unique* RPOs with $T < 3$ that pass reconvergence checks at increased spatial and temporal resolutions; 40 of these satisfy $T < 2$ (and one has $T < 1$).

The paper is laid out as follows: In sections II A to II C we give the necessary background on the fluid dynamical setup, the use of periodic orbits to study such systems and generative diffusion models, respectively. In section III we describe how we generate data to train our diffusion model, the architecture for this model and how it is used to generate synthetic trajectories, and how these trajectories are refined into true solutions. In sections IV A and IV B we give our results for periodic orbits both in the general state space of this system and in a subspace of symmetric vorticity fields. We conclude in section V with implications for invariant-solution studies of turbulence and for physically validated uses of generative modelling.

II. BACKGROUND

A. Two-dimensional Kolmogorov flow

We study the two-dimensional, incompressible Navier-Stokes equations with a sinusoidal forcing,

$$\partial_t u + u\partial_x u + v\partial_y u = -\partial_x p + \frac{1}{Re}\Delta u + \sin 4y, \quad (1)$$

$$\partial_t v + u\partial_x v + v\partial_y v = -\partial_y p + \frac{1}{Re}\Delta v, \quad (2)$$

$$\partial_x u + \partial_y v = 0, \quad (3)$$

solved on a doubly-periodic domain $x \in [0, 2\pi)$, $y \in [0, 2\pi)$. This is one form of Kolmogorov flow, which has been used numerous times as a model for turbulence in a computationally amenable configuration [19–23]. Similar flows have also been studied experimentally [24, 25]. It is important to stress that, although these are indeed the incompressible Navier-Stokes equations, the resulting 2D spatio-temporal chaos is much simpler and quite different in behaviour from fully-developed 3D turbulence.

The equations given above are in the ‘primitive variables’ formulation, describing the horizontal and vertical components of the fluid velocity as u and v and the pressure as p . This form of the problem is both intuitive and computationally efficient [9]. However, for an incompressible two-dimensional flow, these three variables can be reduced to the single variable of vorticity $\omega = \partial_x v - \partial_y u$, so that $u = -\partial_y \Delta^{-1}\omega$, $v = \partial_x \Delta^{-1}\omega$ and $p = -\Delta^{-1}(u_x u_x + v_y v_y + 2u_y v_x)$ with a suitably defined inverse Laplacian Δ^{-1} . By integrating (1) and (2) over the full periodic domain, we see that the spatially averaged horizontal and vertical velocities are conserved quantities of the system, which we shall always take to be zero. This provides the boundary conditions for the inverse Laplacian. Therefore, we arrive at the alternative streamfunction-vorticity formulation for the system:

$$\partial_t \omega + \partial_y \psi \partial_x \omega - \partial_x \psi \partial_y \omega = \frac{1}{Re}\Delta \omega - 4 \cos 4y, \quad (4)$$

$$\psi = -\Delta^{-1}\omega. \quad (5)$$

Here, the flow at a given time is precisely defined by just one field, the vorticity (while also introducing the streamfunction ψ – a dummy variable – for notational clarity). This single variable form will be used throughout, in the direct solution of the evolution equations, and also to train the neural network described in section III B. In a previous study [9], we showed that the primitive variables formulation was more efficient for converging periodic orbits, but in the present work we employ a different method with an explicit Jacobian, and so to reduce memory consumption, we also work directly with the vorticity field in the convergence of periodic orbits, as discussed below.

Using the vorticity, the rate of energy dissipation and production are conveniently defined as, respectively,

$$D = \frac{8}{Re^2 \pi^2} \int_0^{2\pi} \int_0^{2\pi} \omega^2 dx dy \quad (6)$$

and

$$P = -\frac{2}{Re \pi^2} \int_0^{2\pi} \int_0^{2\pi} \omega \cos 4y dx dy, \quad (7)$$

where, following previous authors, these quantities have been normalized so that $D = P = 1$ for the laminar solution $\omega = -\frac{Re}{4} \cos 4y$. The energy dissipation and production must balance over time, so that, for any exact solution to the equations, the time average of D equals the time average of P .

Throughout, we take $Re = 40$. This follows previous studies [5–7, 9], and is modestly above the onset of spatiotemporal chaos at $Re \approx 31.5$. Previous authors have also studied higher values, up to $Re = 400$ [26]. However, since the dynamics have not yet been fully captured at $Re = 40$, it seems unnecessary to expend the significant computational resources required to accurately probe higher values until we have a strategy which works at $Re = 40$. Furthermore, some evidence suggests that the dynamics is actually more complicated at $Re = 40$ than at higher values [27]. One notable feature of the dynamics in this regime is that states spend the majority of their time at low values of dissipation, but occasionally burst to much higher values, as visible in fig. 1.

To solve eqs. (4) and (5), we follow Chandler and Kerswell [5] in employing Heun’s method with the Crank-Nicolson discretisation of the linear dissipative term. We use variously $N = 64$, $N = 96$ or $N = 128$ Fourier modes in both the x and y directions, depending on the desired accuracy.

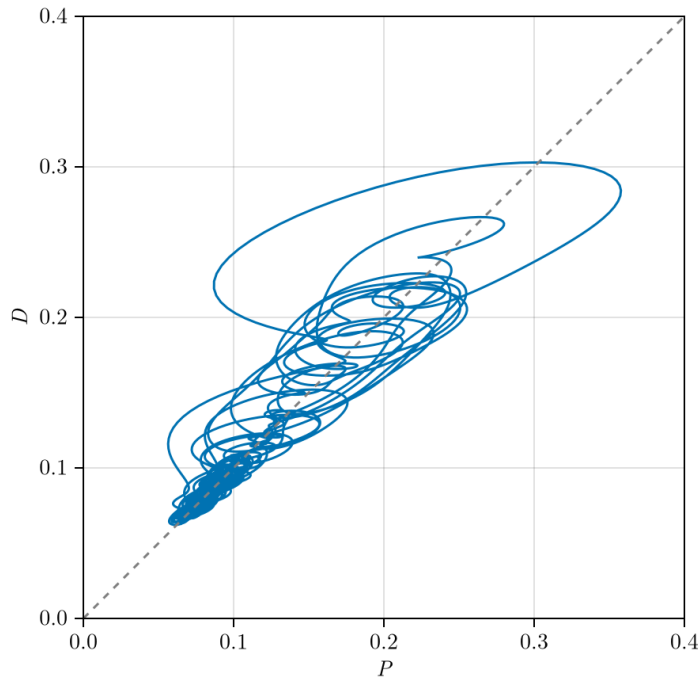


FIG. 1. The rate of energy dissipation D against production P for a typical chaotic trajectory of length $T = 500$. The trajectory spends the overwhelming majority of the time at low dissipations, with $D \leq 0.15$, but occasional ‘bursts’ to higher D are visible.

A symmetry of the system (4)-(5) is a transformation of vorticity fields $\omega \mapsto \omega'$ such that given any solution $\omega(x, y, t)$ to the equations, $\omega'(x, y, t)$ is also a solution. With this particular choice of forcing, the system is invariant with respect to three distinct transformations, which together generate the symmetry group for the system. These are rotation through π ,

$$\mathcal{R} : \omega(x, y) \mapsto \omega(-x, -y), \quad (8)$$

a shift in the y direction by $\pi/4$, reflection in x and a change of sign,

$$\mathcal{S} : \omega(x, y) \mapsto -\omega(-x, y + \pi/4), \quad (9)$$

and a shift by an arbitrary distance s in the x direction (modulo the periodic boundary conditions)

$$\mathcal{T}^s : \omega(x, y) \mapsto \omega(x + s, y). \quad (10)$$

These have inverses $\mathcal{R}^{-1} = \mathcal{R}$, $\mathcal{S}^{-1} = \mathcal{S}^7$ and $(\mathcal{T}^s)^{-1} = \mathcal{T}^{-s}$. Note that these transformations do not commute in general. Any element in the symmetry group can be expressed uniquely in the form $\mathcal{T}^s \mathcal{R}^a \mathcal{S}^m$ where $s \in [0, 2\pi)$, $a \in \{0, 1\}$ and $m \in \{0, \dots, 7\}$. More details can be found in appendix A.

Symmetries affect our problem in several ways: Firstly, given any generic solution, periodic or otherwise, we can find other, equivalent solutions by applying the symmetry operations. We can also find solutions which are periodic modulo the symmetry, as discussed in the next section. Finally, a solution can itself be symmetric. If a vorticity field is invariant under a symmetry transformation, then the trajectory evolving from this field maintains that invariance for all time. Considering all possible symmetries in the group gives rise to an infinite number of invariant subspaces – subsets of the full state space that trajectories can never enter or leave. We will mainly consider the full state space, but section IV B examines the solutions that are invariant under \mathcal{R} , i.e. vorticity fields invariant under rotation by π . This is analogous to studying antisymmetric solutions in another common model system for POs, the Kuramoto-Sivashinsky equation [28, 29]. Authors often concentrate on antisymmetric solutions to reduce the complexity of the problem, even though these solutions are not a priori relevant to the chaotic attractor of the unconstrained system.

B. Periodic orbits

A *periodic orbit* (PO) of the system (4)-(5) is a non-stationary trajectory $\omega(x, y, t)$ such that $\omega(x, y, t+T) = \omega(x, y, t)$ for all x, y and t , for some $T > 0$. If the vorticity field is constant for all t then this is instead an *equilibrium*, and given the existence of the continuous symmetry, we also discount trajectories for which

$$\omega(x, y, t) = \omega(x - ct, y, 0) \quad (11)$$

for some $c \neq 0$ and all t , which are called *travelling waves* (TWs) with respect to the shift symmetry \mathcal{T}^s . Given the existence of the continuous symmetry in this system, true periodic orbits are expected to be vanishingly rare [28]. Instead, we expect *relative periodic orbits* (RPOs), which are trajectories such that

$$\omega(x, y, t + T) = \mathcal{G}\omega(x, y, t) \quad (12)$$

for some symmetry \mathcal{G} . We say that this trajectory is an RPO relative to \mathcal{G} with period T . If \mathcal{G} is a discrete symmetry then this trajectory is also a full periodic orbit with period given by some integer multiple of T (hence some authors refer to these as ‘pre-periodic’ orbits), but we always focus on the shortest possible T .

Though the discrete symmetries of the system form a group of order 16, it is in fact sufficient to consider only 7 different discrete symmetries for the RPOs. This is due to the fact that an RPO relative to one symmetry can be mapped onto another by applying some other symmetry transformations. For example, if there is some initial condition $\omega(x, y, 0)$ such that after a time T it satisfies

$$\mathcal{S}^6\omega(x, y, T) = \omega(x, y, 0), \quad (13)$$

then by letting $\omega'(x, y, 0) = \mathcal{R}\omega(x, y, 0)$, we have

$$\mathcal{S}^2\omega'(x, y, T) = \omega'(x, y, 0), \quad (14)$$

so we do not need to consider \mathcal{S}^6 as well as \mathcal{S}^2 . We will only search for RPOs relative to $\mathcal{T}^s\mathcal{R}^a\mathcal{S}^m$ with

$$(a, m) \in \{(0, 0), (0, 1), (0, 2), (0, 3), (0, 4), (1, 0), (1, 1)\}, \quad s \in \begin{cases} [0, 2\pi), & a + m \text{ even,} \\ \{0\}, & a + m \text{ odd.} \end{cases}$$

A full justification is given in appendix A.

It is important to emphasize the difference between an RPO relative to some symmetry and a PO in a symmetric subspace. The two can be combined – there are RPOs in symmetric subspaces; the concepts are related but distinct. In general, the existence of a continuous symmetry means that RPOs are crucial for understanding the dynamics [28], but when restricted to a symmetric subspace, this is no longer the case [29].

The interest in finding POs in turbulence was motivated by *periodic orbit theory*, which is a mathematically justified approach to studying certain classes of chaotic dynamical systems [30–32]. A statistical average of a physical observable of interest can be expanded as a sum of the observable evaluated over all the periodic orbits within the chaotic attractor, combined with suitable weights which encode the relative importance of each individual PO. For this to be a practically useful avenue of research, one must know how many terms need to be included in finite truncations of this infinite sum for a desired level of accuracy. By analogy: one can always write down a Taylor expansion for a function, but this is only useful if one has an upper bound on the size of the remainder after the series has been truncated. In simple systems, including many classical chaotic ODEs but also the simple chaotic PDE of the Kuramoto-Sivshinsky equation [28, 33, 34], chaotic attractors have been found with a clear hierarchy of POs – there are a small number of particularly short orbits, which encode the overwhelming majority of the dynamics of system, and can be combined to create all the longer orbits. These short orbits also provide the basis of the *symbolic dynamics* which understands the continuous dynamical system as a discrete Markov process in a rigorous way. The hope is that such interpretation is possible for ‘turbulence’ at least in small domains, but turbulence by its nature is defined by spatiotemporal chaos and a large number of positive Lyapunov exponents which, to-date, periodic orbit theory has failed to tame in a mathematically justified way. Even with two positive Lyapunov exponents, results from periodic orbit theory are limited, though there has been some success finding symbolic dynamics [35]. Nevertheless, periodic orbits have captured some of the statistical behaviour of turbulent flows with very small numbers of periodic orbits, or even a single one [36].

In 2D Kolmogorov flow, the hunt for POs and RPOs began with Chandler and Kerswell [5], who found 3 POs and 55 RPOs at $Re = 40$ and used these with various ad hoc choices of weights to try to recreate the statistics of the flow. Subsequent authors have found hundreds more orbits [6–9] and attempted to better reproduce the statistics of the

flow using weights derived by modern machine learning techniques [7] in order accurately recreate the distribution of dissipation, but no studies have detected any hint of the clear hierarchy of states necessary to build a complete, rigorously justified, periodic orbit expansion. Indeed, no studies to-date have focused on finding the very shortest orbits which would be the building blocks for such a hierarchy. In fact, save for the original Chandler and Kerswell [5] study which looked for solutions with a vertical shift, no studies have attempted to find RPOs with any other symmetry properties than a simple horizontal shift. To the best of our knowledge, only three orbits with period $T < 2$ have previously been found, all of them by Page *et al.* [8] and all of them with extremely high average dissipation, at least one half of the dissipation of the laminar state. It is possible that other short orbits have been found, but only as undetected multiple traversals of RPOs. The purpose of the present work is to attempt to find structure in the RPOs of this system: to find the shortest periodic orbits in Kolmogorov flow, relative to all possible symmetries of the system.

C. Diffusion models

Diffusion models are a family of generative machine learning approaches originally conceived to generate images. Unlike the earlier methods of generative adversarial networks [37] and variational autoencoders [38], one single neural network does not generate a full image. Instead, a convolutional neural network is trained to predict the pattern of noise which has been added to a set of noise-free training images. Conceptually, a diffusion model consists of two parts: a forward process, where random noise is incrementally added to the data following some predefined statistical process, and a reverse process, where a neural network, trained on a large dataset, predicts the noise which has been added, and which can then be subtracted to reproduce the original clean image. Then, starting instead with pure noise as input, the reverse process can be used to generate entirely synthetic images which match those in the training set. Introduced by Sohl-Dickstein *et al.* [39], diffusion models were initially overlooked due to computational inefficiencies but have since been revitalized through major innovations in training and sampling [40].

Different variants of diffusion models have been developed to address challenges such as computational expense and sampling efficiency. Denoising Diffusion Probabilistic Models (DDPMs), popularised by Ho *et al.* [40], refine the reverse process stochastically, producing high-quality samples at the cost of requiring thousands of individual sampling steps. Their robust training dynamics and strong performance have made them a benchmark for diffusion-based generative models. Denoising Diffusion Implicit Models (DDIMs) [41] improve upon DDPMs by reformulating the reverse process to allow deterministic sampling. This not only reduces the number of steps required for data generation but also introduces more control over the sampling process. We employ a DDIM in this work.

In the forward process, normally distributed noise $\epsilon \sim \mathcal{N}(0, 1)$ is added to the original data z^0 via a fixed decreasing $\alpha_\tau \in (0, 1]$ depending on the ‘timestep’ τ ,

$$z^\tau = \sqrt{\alpha_\tau} z^0 + \sqrt{1 - \alpha_\tau} \epsilon, \quad (15)$$

up to some final time $\tau = N_\tau$ for which $\alpha_\tau \approx 0$, giving almost pure noise. This forward process is identical to that of DDPMs. At each timestep of the reverse process, the model predicts the denoised version of the data, \hat{z}^0 , from the noisy intermediate state \hat{z}^τ as

$$\hat{z}^0 = \frac{\hat{z}^\tau - \sqrt{1 - \alpha_\tau} \hat{\epsilon}(\hat{z}^\tau, \tau)}{\sqrt{\alpha_\tau}}, \quad (16)$$

where $\hat{\epsilon}$ is a neural network that estimates the added noise given the noisy data. Using this estimate, DDIMs predict the next state in the denoising process,

$$\hat{z}^{\tau - \delta\tau} = \sqrt{\alpha_{\tau - \delta\tau}} \hat{z}^0 + \sqrt{1 - \alpha_{\tau - \delta\tau}} \hat{\epsilon}(\hat{z}^\tau, \tau). \quad (17)$$

This deterministic update rule allows DDIMs to generate high-fidelity samples with fewer steps than DDPMs, if $\delta\tau > 1$.

III. METHODS

A. Data generation

A long time-series of the chaotic attractor was computed at $Re = 40$ using a $N \times N = 128 \times 128$ spatial resolution, and a timestep of $\delta t = 0.005$, using the numerical scheme mentioned in section II A. For training the diffusion model,

these data were downsampled to $N \times N = 64 \times 64$ and $\delta t = 0.02$, since the very fine scales required for accurate solution of the Navier-Stokes equations are presumed to be unimportant for the large-scale patterns we are trying to imitate.

Initial attempts to find periodic orbits resulted in a very large number of steady-state equilibrium solutions. This is likely due to the fact that, for most of the time, the Kolmogorov flow remains very close to the low-dissipation E1 solution [5]. To mitigate this, we instead trained our diffusion model only on high-dissipation events. Specifically, the time-series – after an initial spin-up period of $T = 1000$ was discarded – was split into blocks of length $T = 10.24$, corresponding to $M = 512$ slices. Note that this is significantly longer than the individual periodic orbits we are targeting, allowing time for the dynamics to explore multiple solutions in a single block. A block was only included in our training data if, somewhere within this block, the instantaneous dissipation was measured to be $D > 0.15$. This cut-off value of $D = 0.15$ was used by Page *et al.* [42] to detect high-dissipation ‘bursting’ events, and by this definition, all of our training data therefore contains a burst.

B. Equivariant DDIM

Aside from the specific neural network architecture detailed below for our application, we used a standard DDIM [41]. We used the Adam optimizer with fixed learning rate 5×10^{-5} . The DDIM used a total of $N_\tau = 1000$ steps, and we used 50 evenly spaced steps to generate outputs. Following Ho *et al.* [40], the variance schedule β_τ increases linearly from $\beta_1 = 10^{-4}$ to $\beta_{1000} = 0.02$, and then α_τ is calculated as

$$\alpha_\tau = \prod_{s=1}^{\tau} (1 - \beta_s). \quad (18)$$

In order to be able to generate time-series with any desired number of timesteps, and potentially different spatial sizes too, we use a fully-convolutional network, as any densely connected layer would force a particular resolution. One option would be a simple stack of convolutions which all preserve the size of the input. However, in order to more efficiently model large-scale features, we use a U-net architecture [43], which downsamples and then subsequently upsamples the resolution in both the two spatial dimensions and in time. In fact, because of this downsampling, with the particular U-net described below, this choice restricts the time resolution to be a multiple of 8 and the spatial resolution to be a multiple of 16, but this was not found to be a significant restriction in practice.

Let the input noise field be denoted z_{ijk} , where $1 \leq i \leq N$, $1 \leq j \leq N$ and $1 \leq k \leq M$. The neural network is a function $\hat{\epsilon} : \mathbb{R}^{N \times N \times M} \times \mathbb{N} \rightarrow \mathbb{R}^{N \times N \times M}$, with the goal being that the final evaluation of the DDIM

$$\hat{z}^0 = \frac{\hat{z}^\tau - \sqrt{1 - \alpha_\tau} \hat{\epsilon}(\hat{z}^\tau, \tau)}{\sqrt{\alpha_\tau}}, \quad (19)$$

gives a vorticity time-series

$$\omega((2i-1)\pi/N, (2j-1)\pi/N, k\delta t) = \hat{z}_{i,j,k}^0$$

which approximately satisfies eq. (4).

A fully-convolutional network automatically has many properties we would like: the network is agnostic to the shape of the input, and shifting in time or space does not alter the results. The design of the network is strongly constrained by the fact that we wish to be able to generate periodic orbits, and relative periodic orbits with various symmetries: suppose hypothetically that the input to the network were an infinitely long sequence of $N \times N$ slices, so that $\hat{\epsilon} : \mathbb{R}^{N \times N \times \mathbb{Z}} \times \mathbb{N} \rightarrow \mathbb{R}^{N \times N \times \mathbb{Z}}$. Since the network downsamples the inputs by a factor of 8, it cannot be the case that shifting the input by 1 in the time direction results in the same output but perfectly shifted by 1. However, by careful choice of the convolution, downsampling and upsampling operations, we can ensure that shifting the inputs by 8 in time gives an identical output, but shifted by 8. That is to say, letting $z'_{i,j,k} = z_{i,j,k+8}$, we have

$$(\hat{\epsilon}(z', \tau))_{i,j,k} = (\hat{\epsilon}(z, \tau))_{i,j,k+8}. \quad (20)$$

In this way, the final generated guess for a vorticity field would also have this shift symmetry. In order for this to hold, all convolutions have a stride of 1. The usual max-pooling for downsampling would break the symmetry \mathcal{S} we wish to preserve, so instead we opt for $2 \times 2 \times 2$ average pooling throughout, and we perform upsampling with a custom trilinear interpolation. With these choices, suppose that the input were periodic with period $8K$ for some K , i.e. $z_{i,j,k+8K} = z_{i,j,k}$. Then

$$(\hat{\epsilon}(z, \tau))_{i,j,k+8K} = (\hat{\epsilon}(z, \tau))_{i,j,k}, \quad (21)$$

for every τ and therefore the generated vorticity field satisfies

$$\omega(x, y, t + 8K\delta_t) = \omega(x, y, t), \quad (22)$$

a synthetic periodic orbit with period $8K\delta_t$. Furthermore, we wish to preserve the symmetries of the system described in section II A. That is to say, given an element \mathcal{G} in the symmetry group, the function $\hat{\epsilon}$ should be equivariant with respect to the action of g on inputs z

$$\hat{\epsilon}(\mathcal{G}z, \tau) = \mathcal{G}\hat{\epsilon}(z, \tau), \quad (23)$$

for all z and τ .

One important consideration for this to hold is how we handle the input τ , which is the current ‘timestep’ of the diffusion process. (This is unrelated to the timestep of the spatiotemporal field z , which encodes time in its third dimension.) Typically in DDPMs and DDIMs this is done with some form of positional encoding, which encodes the integer τ as a series of sines and cosines, which are then input into a small multilayer perceptron (MLP) which can learn a suitable representation of this for the network [40, 44]. We follow this procedure, but in order to feed this information into every layer of the network while still preserving the symmetries, this embedded time is multiplied by the forcing field $f_{i,j,k} = -4 \cos\left(\frac{4(2j-1)\pi}{N}\right)$, and this tensor is then concatenated onto the inputs to every convolutional block in the network. Using the forcing field in this way has the added benefit of breaking continuous translational symmetry in the y direction, which is not a symmetry of our equations but which would otherwise have been a symmetry of the fully convolutional neural network with periodic boundary conditions.

The continuous symmetry in the x -direction becomes, in this discretized representation,

$$(\mathcal{T}_l z)_{i,j,k} = z_{i+\frac{lN}{2\pi},j,k}$$

so long as the shift l is an exact multiple of $2\pi/N$. (Of course in this case it is not a continuous symmetry, but is approximately so when N is large.) Here, indices outside of the range $1 \leq i \leq N$ are understood periodically. The equivariance $\hat{\epsilon}(\mathcal{T}_l z) = \mathcal{T}_l \hat{\epsilon}(z)$ is a natural consequence of a fully convolutional network, so long as the discrete convolutions are padded with periodic padding in the x direction. We also use periodic padding in the y direction, but shifts by arbitrary amounts in this direction are not equivariant, since the constant forcing field f is not itself invariant under arbitrary y shifts.

The rotation symmetry \mathcal{R} is also straightforward to handle: all kernels of the convolution layers must themselves be invariant under a rotation through π . The shift-and-reflect symmetry \mathcal{S} is somewhat more complicated to incorporate into the neural network architecture. For \mathcal{S}^m with m even, it reduces to a simple translation in y by $mN/8$, and this is captured automatically via the periodic padding and the fact that the forcing field satisfies $\mathcal{S}^2 f = f$. However, when m is odd, the symmetry introduces a change of sign to the output. One option would be for all activation layers σ in the neural network to satisfy $\sigma(-z_{ijk}) = -\sigma(z_{ijk})$, and this, combined with the fact that all other layers (convolutions, average pooling and trilinear upsampling) are purely linear, would mean that $\hat{\epsilon}(-z) = -\hat{\epsilon}(z)$. But pure change-of-sign is not a symmetry of eq. (4) – it is not the case that given a solution $\omega(x, y, t)$, another is given by $-\omega(x, y, t)$. Therefore, such a choice would put an additional restriction on the neural network which is unnatural and would lead to poor performance and generalisation. Instead, we must take into account the reflection in x .

To proceed, let us examine the individual terms of (4). The time derivative and Laplacian terms are purely linear in ω , and thus equivariant under a change of sign. Additionally, these terms are equivariant under reflection in x , as the former has no spatial derivatives and the latter has a second derivative in x . The nonlinear terms $\partial_y \psi \partial_x \omega$ and $\partial_x \psi \partial_y \omega$ are completely different: they are *invariant* under a change of sign of ω (since $\psi = -\Delta^{-1}\omega$ changes sign with ω) and change sign under reflection in x , since each term has one derivative in x . This inspires handling these two modes of symmetry in parallel in our neural network: either we have (a) a convolution which is symmetric in x and an activation which is an odd function (i.e. equivariant under a change of sign) or we have (b) an even function followed by a convolution which is antisymmetric in x and then an odd activation function. Type (a) operations are invariant under reflection and equivariant under change of sign, and vice-versa for type (b). If we combine both of these operations in one neural network, the result will be equivariant under reflection in x and change of sign simultaneously, but will have no special symmetry if either of these operations is applied individually.

Convolutions of type (a) have kernels which are symmetric in the first dimension and also symmetric under rotation by π , as required for equivariance under \mathcal{R} . For a 5×5 filter this leaves 9 unique elements. Convolutions of type (b) have kernels anti-symmetric in the first dimension but still symmetric under rotation by π , which leaves just four unique element for 5×5 convolutions. This is depicted graphically in figure 2. In practice, we also perform a convolution in time, with no symmetry restrictions in that direction, so for $5 \times 5 \times 5$ convolutions, we have 45 parameters for type (a) and 20 for type (b). Further to this, the convolutions are performed across a variable number

$$\begin{array}{c}
\begin{pmatrix} a_1 & a_2 & a_3 & a_2 & a_1 \\ a_4 & a_5 & a_6 & a_5 & a_4 \\ a_7 & a_8 & a_9 & a_8 & a_7 \\ a_4 & a_5 & a_6 & a_5 & a_4 \\ a_1 & a_2 & a_3 & a_2 & a_1 \end{pmatrix} \\
\text{(a)}
\end{array}
\qquad
\begin{array}{c}
\begin{pmatrix} b_1 & b_2 & 0 & -b_2 & -b_1 \\ b_3 & b_4 & 0 & -b_4 & -b_3 \\ 0 & 0 & 0 & 0 & 0 \\ -b_3 & -b_4 & 0 & b_4 & b_3 \\ -b_1 & -b_2 & 0 & b_2 & b_1 \end{pmatrix} \\
\text{(b)}
\end{array}$$

FIG. 2. The symmetric structure of the kernels for convolutions of type (a) and (b), assuming a size 5×5 , with respectively 9 and 4 unique elements. In practice the kernels are $5 \times 5 \times 5 \times d_i \times d_o$ arrays, but no special structure is imposed in the third (time) dimension, nor in the dimensions covering the number of input and output channels d_i and d_o .

of input channels and output channels, so the number of parameters rapidly becomes very large, though still much smaller than if these symmetry constraints were not imposed on the convolutions.

Many neural networks make use of ReLU activation functions or modifications thereof, which are computationally efficient and do not suffer from saturation. However, this family of functions are neither even nor odd, so cannot be used if we wish to preserve symmetries. The widely used hyperbolic tangent activation is an odd function, but suffers from vanishing gradients. For this reason we use an activation function $\text{tanhshrink}(x) = x - \tanh x$ [45] after all convolutions. For the even function required before the convolution in type (b) operations, we use a function $\text{softabs}(x) = \frac{|x|^3}{0.1+x^2}$, which approximates the usual absolute value with an everywhere-differentiable function.

Putting these together, the neural network is assembled from convolutional blocks containing parallel type (a) and (b) convolutions with their respective activations, concatenation, followed by a set of convolutions and concatenation. Performance was observed to increase with the inclusion of a residual connection past the convolutions which is then added to the output of the block, and also the use of group normalisation after each of the concatenations. The full convolutional block is depicted in fig. 3.

The full structure of the U-Net for $\hat{\epsilon}$ is depicted in fig. 4, and the full source code, implemented with Keras/Tensorflow with several custom layers, is available at https://github.com/jeremyparker/Parker_Schneider_Diffusion_Model.

1. Padding

To preserve the size before and after a discrete convolution, the inputs must be padded. With the $5 \times 5 \times 5$ kernels we use, this means that two elements must be augmented to the data on either side of the first three dimensions. In all cases we use periodic padding in both spatial dimensions to represent the periodic boundary conditions of the PDE. That is, the first two rows/columns of each slice are appended to the opposite side, and likewise with the final two. In the third, temporal dimension, we must be more careful. The training data (discussed in section III A) is not periodic in time, and therefore using periodic padding would result in a discontinuity. Zero padding is common in image processing tasks where the mean is subtracted from the data at each layer, but since we are not doing this, we instead use mirror padding in the third dimension during training. That is, the last two slices are swapped and appended to the end, and similarly the first two slices at the start.

During the generation phase of our method, we aim to create synthetic trajectories which are explicitly periodic in time, or periodic relative to a transformation in the symmetry group of the system. In the former case, of non-relative periodic orbits, these can be generated by simply using normal periodic padding in the third dimension as in the first two dimensions. We only do this in the \mathcal{R} -invariant subspace as described in section IV B, in all other cases we are concerned with non-trivial symmetry transformations, which requires a custom padding operation. In cases where the transformation $\mathcal{T}^s \mathcal{R}^a \mathcal{S}^m$ has $s = 0$, consisting only of rotations, reflections and discrete vertical shifts, this can be done exactly: We pad the end of the third dimension with the first two slices, transformed by $\mathcal{T}^s \mathcal{R}^a \mathcal{S}^m$, and we pad the start with the final two slices transformed by the inverse operation. When $s \neq 0$, we do exactly the same, but in this case we must use linear interpolation to handle arbitrary shifts in the x direction, which introduces some small artifacts in the generated synthetic orbits as arbitrary shifts in the x direction are not an equivariance of the neural network (unless the shift s is an integer multiple of $\pi/8$).

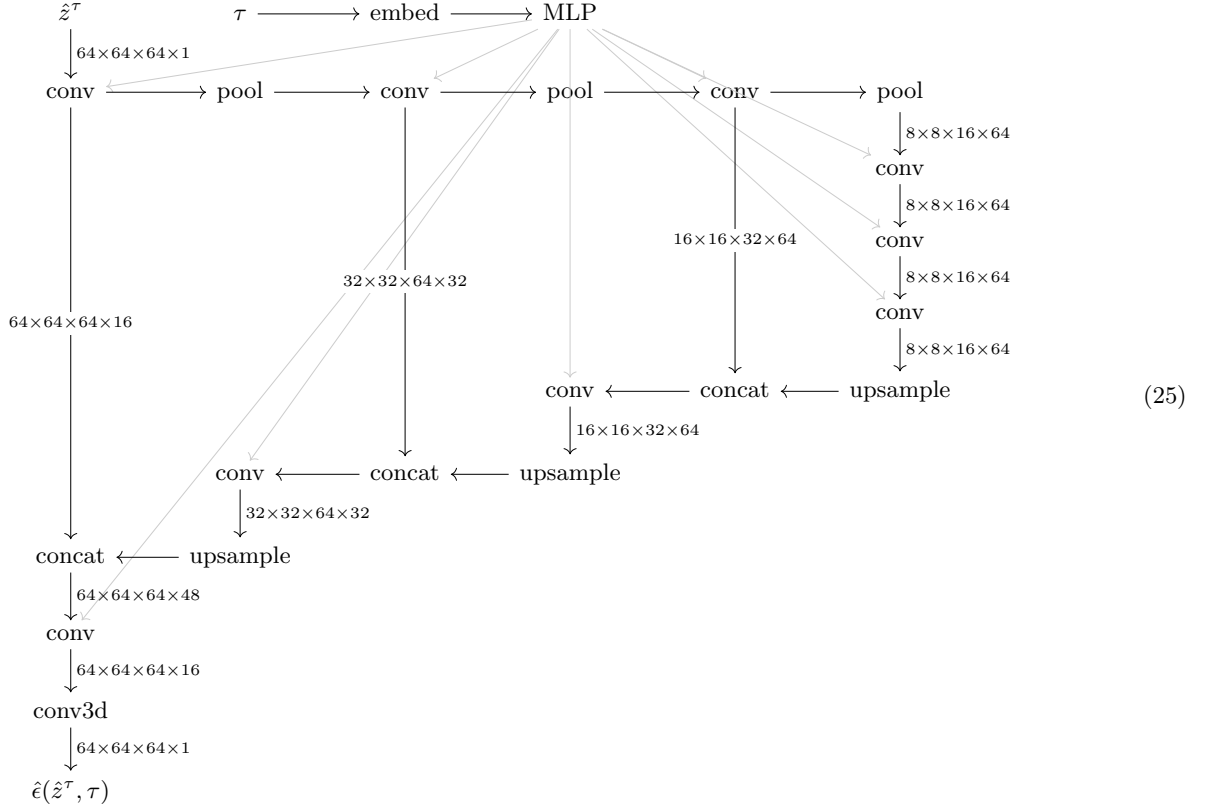


FIG. 4. The structure of the equivariant U-Net used by the diffusion model. Each conv block is as per fig. 3. We use average pooling and trilinear upsampling. The concatenation is along the 4th dimension. The sizes given are those used during generation; during training, all layers were 8 times larger in the third dimension.

One subtlety is that our diffusion model acts on grids of datapoints, whereas our convergence algorithm operates entirely on Fourier coefficients in the two spatial directions, except for a pseudo-spectral collocation step to handle the nonlinearity. This collocation uses gridpoints at $x = 0, 2\pi/N, \dots$, allowing the symmetry operations to be performed efficiently in Fourier space. The neural network, by contrast, expects datapoints at $x = \frac{1}{2} \times 2\pi/N, \frac{3}{2} \times 2\pi/N, \dots$, which means, for example, that \mathcal{R} is simply a rotation of the whole image. This necessitates a half-pixel shift when the synthetic orbits are used as initial guesses for the convergence algorithm, which results in a small loss of accuracy.

IV. RESULTS

A. Full state space

For each of the 7 unique classes of RPO, we generated 400 synthetic orbits using the diffusion model, with $(N, M) = (64, 64)$. Since $\delta t = 0.02$, $M = 64$ corresponds to RPOs of length $T = 1.28$, which is less than every previously known RPO for this system. This was chosen in order to force the method to find the very shortest solutions.

Examples of the resulting synthetic orbits are plotted in fig. 5. These show only a very weak correlation, if any, between the average values of D and P , which must be equal for any true solution. However, there is clear evidence that the network has learnt that dissipation varies much less than production on any given orbit, as visible in the short and wide oval shapes. All our synthetic orbits have medium values of dissipation, and there is no clear pattern between the synthetic orbits of the different symmetries. Crucially, we have not been able to generate orbits of very low dissipation which have historically been the most common ones found by previous studies. This is partly due to the short periods we are targeting, and the fact that our model was trained only on high-dissipation bursting events, as discussed in section III A.

The synthetic trajectories were used as initial guesses for the convergence algorithm described in section III C.

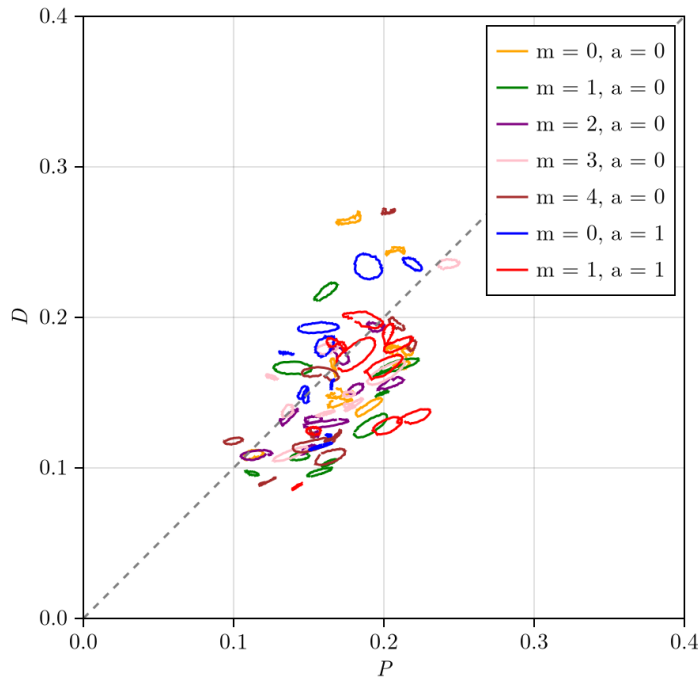


FIG. 5. Energy dissipation D versus production P for synthetic orbits generated with $(N, M) = (64, 64)$. Ten examples from each of the symmetries are shown. The examples were chosen at random: many of these converged to true solutions, many did not.

m	a	Generated	Did not converge	Equilibria/ TWs	Too long	Unique candidates	Converged RPOs
0	0	400	345	4	41	9	9
1	0	400	285	21	35	32	21
2	0	400	344	4	33	17	13
3	0	400	311	10	29	31	23
4	0	400	287	21	67	22	16
0	1	400	276	39	52	28	21
1	1	400	355	4	28	13	8
		2800	2203	103	285	152	111

TABLE I. The number of solutions converged for each of the 7 distinct classes of symmetry. More than 20% of the generated synthetic orbits converged at low resolution, but many of these converged to equilibria or travelling waves, to period orbits with $T > 3$, or to duplicates of one another. The unique converged candidates were then reconverged at higher resolution, giving the totals in the final column.

Of these 2800 guesses, 597 converged to a relative error of less than 10^{-6} , though 103 of these were apparently equilibrium or travelling wave solutions and were not considered further. 285 ‘converged’ to orbits with period $T > 3$ and were not considered further, both because we are most interested in short orbits but also because $M = 64$ is likely to be underresolved and thus the results unreliable when $T \gg 3$. A further 57 orbits were detected to be duplicates and therefore discarded. The remaining 152 orbits were then reconverged at both $(N, M) = (64, 128)$ and $(N, M) = (96, 64)$ – it being too memory intensive to increase in both dimensions simultaneously – to check that the values were not sensitive to the discretisation. In total, 111 unique RPOs with $T < 3$ were found for which the reconvergence at the two different increased resolutions matched, strongly indicating true solutions to the governing equations. Forty of these had $T < 2$, and one of these had $T < 1$, though this latter had extremely high dissipation and is omitted from fig. 8. Figures 6 and 7 show example synthetic orbits and the corresponding converged solutions. In the former case, the solutions are visually very similar to the synthetic guesses, and in the latter they are very different. Most of our successful convergences were between these two extremes, with some clearly related vortices, but with noticeable differences in the details. Table I summarizes the results for each of the symmetry classes. As far as we can tell, none of our solutions were previously known, though it is possible that multiple traversals of these short orbits had been detected by previous authors as longer POs.

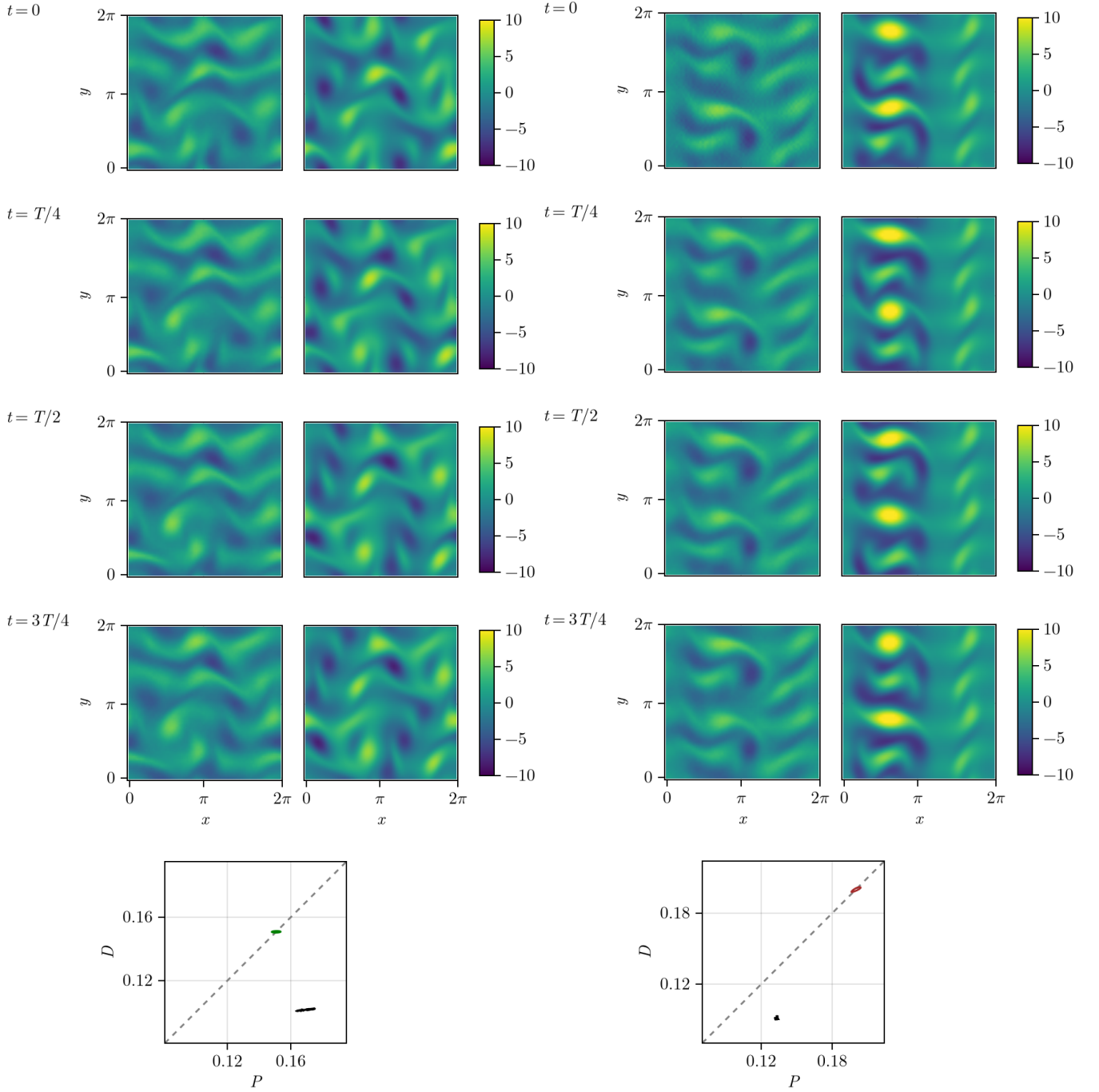


FIG. 6. Examples of synthetic orbits which converged to visually similar solutions. In both cases, the left column depicts vorticity field slices of the synthetic trajectory with $T = 1.28$ and the right column slices of the converged solution of the Navier-Stokes equations. The bottom panel shows the dissipation D against production P for the synthetic (black) and converged (coloured) trajectories. The left example, periodic relative to $\mathcal{T}^s \mathcal{R}^a \mathcal{S}^m$ with $m = 1$ and $a = 0$ converged to a solution with $s = 0$ and $T \approx 1.56$. The right has $m = 4$, $a = 0$, $s \approx -0.02$ and $T \approx 2.46$.

B. \mathcal{R} -invariant solutions

It was observed by Chandler and Kerswell [5] that the \mathcal{R} -invariant subspace seems to be closely visited by chaotic trajectories in the full space. In particular, the most commonly found PO by several studies [5, 50] is invariant under rotation by π . It has period $T \approx 5.38$. It is not an RPO; it has no drift velocity due to its symmetry.

The diffusion model and convergence method presented in this paper will not naturally find solutions in invariant

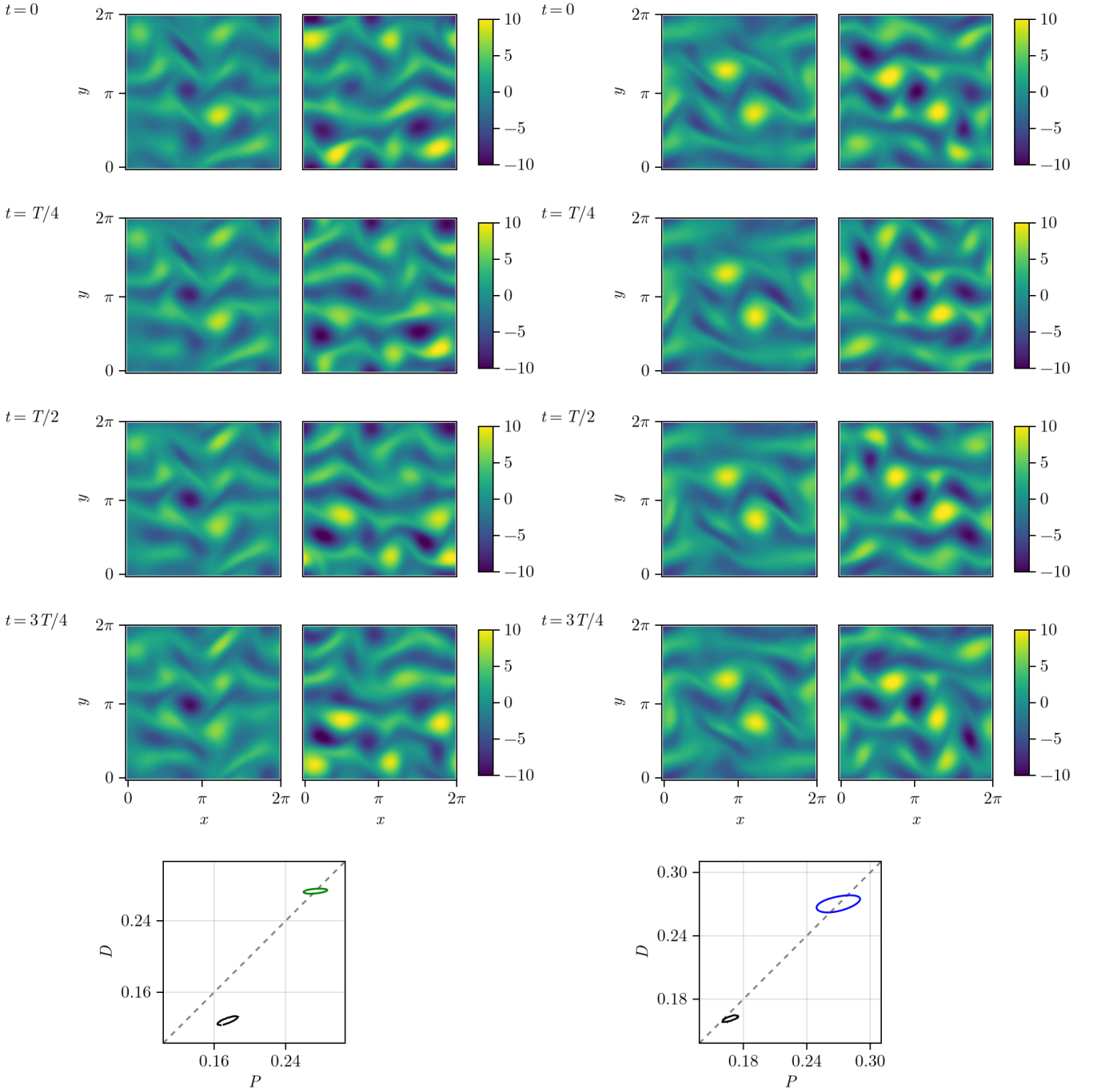


FIG. 7. Examples of synthetic orbits which converged to very different solutions, as per fig. 6. The left example, periodic relative to $\mathcal{T}^s \mathcal{R}^a \mathcal{S}^m$ with $m = 1$ and $a = 0$ converged to a solution with $s = 0$ and $T \approx 2.33$. The right has $m = 0$, $a = 1$, $s = 0$ and $T \approx 2.86$.

subspaces, though several examples in the previous section were close to these, likely representing weak symmetry-breaking of solutions from these invariant subspaces. Because of the symmetry-aware design of the diffusion model, to search directly for \mathcal{R} -invariant POs we can simply use as input for our diffusion model a noise field which itself is invariant under rotation by π . Similarly we could search for POs in any other of the infinitely many symmetric subspaces using this technique.

It is important to note that we did not retrain the network to generate these \mathcal{R} -invariant POs; we used the same weights as in the previous subsection. This means that the dynamics we generate are not likely to be representative of the dynamics in this invariant subspace. Indeed, we did not even verify that the dynamics are chaotic in this case.

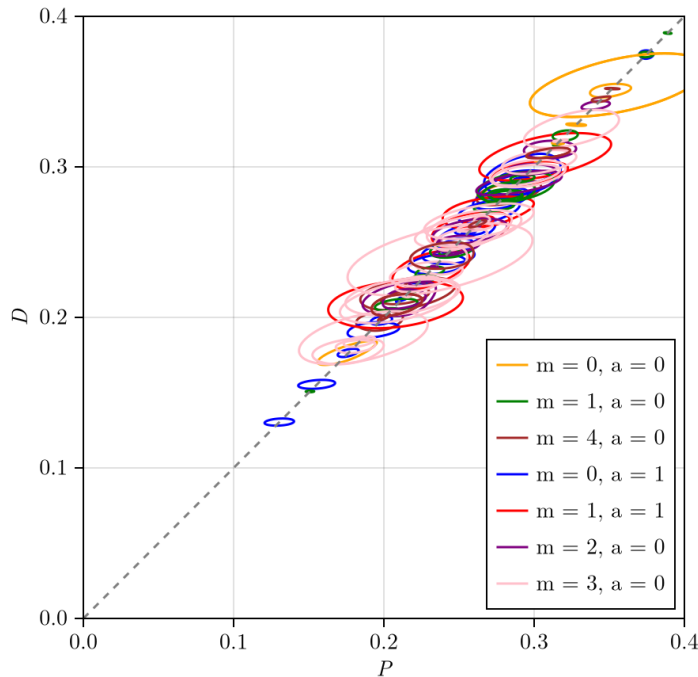


FIG. 8. The rate of energy dissipation D against production P for the successfully converged solutions. The colours show the different symmetry transformations relative to which they are periodic orbits. Compare with fig. 1. Two orbits with $D \approx 0.6$ are excluded from this plot.

Rather, we aim to generate invariant POs which are relevant to the chaotic dynamics of the full space.

As in section IV A, we generated 400 synthetic orbits. For each input to the diffusion model we took a $64 \times 64 \times 64$ unit Gaussian noise field, which was then rotated by π in the spatial dimensions, added to the original and then the result was divided by $\sqrt{2}$ to give an \mathcal{R} invariant noise field matching the same unit standard deviation as the general Gaussian noise fields used to train the model. These noise fields were then subject to backward diffusion in exactly the same way as in section IV A, and the resulting synthetic orbits used as initial guesses for our convergence algorithm.

Of the 400 generated synthetic trajectories, 91 converged to a residual below our cutoff, but 16 of these were equilibria and thus discarded. Of the remaining 75, all but one converged to have period greater than our cut-off of $T = 3$, and this single success converged to an orbit with very high dissipation. When the cut-off was relaxed to $T \leq 4$, a further three likely physical periodic orbits were detected. All four of these were successfully reconverged at $(N, M) = (64, 128)$ and $(N, M) = (96, 64)$. All four of these had high dissipation. Two examples are shown in fig. 10, and the full collection is depicted in fig. 9.

V. DISCUSSION

In this paper, we trained a diffusion model to output time-series which approximate trajectories in 2D turbulence, and then modified the structure (but not the weights) of the underlying neural network to instead generate periodic time-series. We were able to converge a large proportion of these synthetic time-series to true periodic solutions of the Navier-Stokes equations, though in many cases the final solution and the initial guess drastically differ. This suggests that, at least in the form we have presented, the diffusion model is not sufficient to understand the physics of the turbulence, but by combining it with existing numerical methods, we have made a significant advance in this well-studied area. Furthermore, the use of a carefully designed equivariant neural network has allowed us to find solutions with every possible symmetry.

All of the short converged orbits we have found are geometrically very simple, which strongly suggests that they cannot be understood by ‘gluing’ [10] other orbits together and points to the fact that these solutions might be fundamental to understanding the chaotic attractor which underlies the dynamics. It should be noted that it is impossible, given current methods, to know whether all or indeed any of our solutions are actually contained within the chaotic attractor or merely close to it, as is known to occur in some PDE systems [34]. This is an issue common

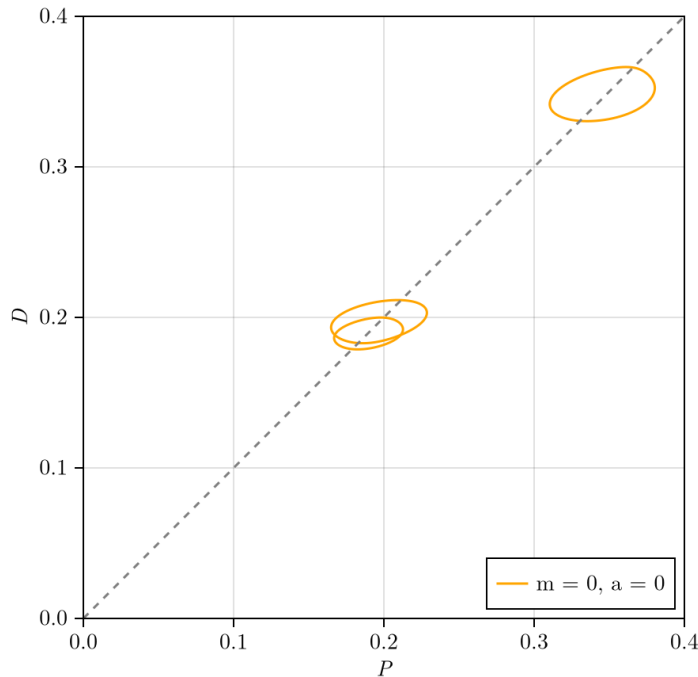


FIG. 9. The dissipation D against energy production P for the successfully converged periodic orbits in the \mathcal{R} -invariant subspace. One orbit with $D \approx 0.7$ is excluded from this plot.

to all similar studies, and we appeal to the large numbers that we have found and the clear similarities to turbulent flows when we draw conclusions from our numerical results.

Assuming that most or all of the 111 orbits we have found are indeed part of the chaotic attractor, their geometric simplicity implies that they each represent a single symbol within a symbolic dynamics for this system. Furthermore, we found relatively few duplicates, and we did not make a concerted effort to find orbits with dissipation $D \leq 0.15$, which suggests that there are at least hundreds, if not thousands, more short orbits to be found. A symbolic dynamics with hundreds or thousands of different symbols is completely unmanageable with current methods, and if we then consider gluing these orbits to find orbits corresponding to sequences of length 2, the computational infeasibility of applying true periodic orbit theory in this problem becomes apparent. This is for a two-dimensional, small-domain flow modestly above the onset of turbulence, which does not bode well for applying periodic orbit theory to three-dimensional turbulence in our generation.

ACKNOWLEDGMENTS

This work was supported by the European Research Council (ERC) under the European Union's Horizon 2020 research and innovation programme (grant no. 865677).

Appendix A: Symmetries

Let \mathcal{U} , \mathcal{X} , \mathcal{Y} and \mathcal{C} represent, respectively, y -shift by $\pi/8$, reflection in x , reflection in y and change of sign of ω . Considering these alongside \mathcal{T}^s , an x -shift by s , as the fundamental transformations of the vorticity field ω , we have the commutation relations $\mathcal{U}\mathcal{Y} = \mathcal{Y}\mathcal{U}^{-1}$ and $\mathcal{X}\mathcal{T}^s = \mathcal{T}^{-s}\mathcal{X}$ and all other combinations commute. Also note that \mathcal{X} , \mathcal{Y} and \mathcal{C} are their own inverses. The basic symmetries of the system, under which eq. (4) is equivariant, are then the discrete symmetries $\mathcal{S} = \mathcal{C}\mathcal{U}\mathcal{X}$ and $\mathcal{R} = \mathcal{X}\mathcal{Y}$ and the continuous symmetry \mathcal{T}^s for any s . (If $2\pi/s$ is a rational number then after raising \mathcal{T}^s to some integer power we recover the identity, so in that sense it is a discrete symmetry, but still belongs to the one-parameter family.)

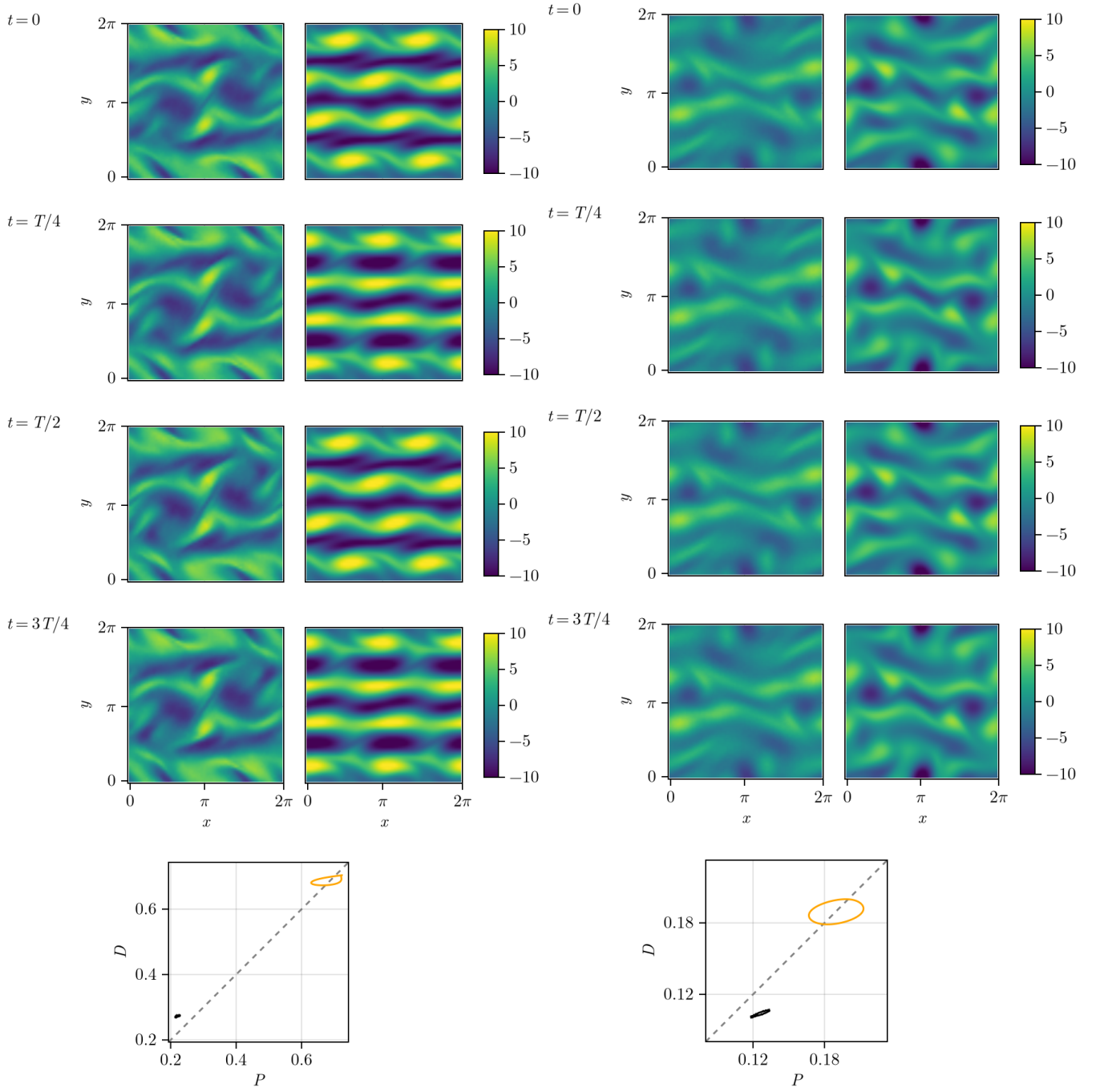


FIG. 10. Successfully converged solutions in the \mathcal{R} -invariant subspace. Left: this synthetic orbit converged to a PO with period $T \approx 2.17$ and the extremely high dissipation $D \approx 0.69$. The converged solution appears to also be invariant under a horizontal shift \mathcal{T}^π , which was certainly not true for the guess. Right: this synthetic orbit converged to a PO with $T \approx 3.90$. The converged result is visually similar to the synthetic orbit, though the dissipation is still somewhat higher.

Using these definitions, we can immediately derive the commutation relations for the symmetries

$$\mathcal{R}\mathcal{S} = \mathcal{S}^{-1}\mathcal{R}, \quad \mathcal{S}\mathcal{R} = \mathcal{R}\mathcal{S}^{-1}, \quad \mathcal{T}^s\mathcal{R} = \mathcal{R}\mathcal{T}^{-s}, \quad \mathcal{T}^s\mathcal{S} = \mathcal{S}\mathcal{T}^{-s}. \quad (\text{A1})$$

The subgroup generated by \mathcal{R} and \mathcal{S} has the presentation

$$\langle \mathcal{R}, \mathcal{S} \mid \mathcal{R}^2, \mathcal{S}^8, (\mathcal{R}\mathcal{S})^2 \rangle \cong D_8, \quad (\text{A2})$$

isomorphic to the dihedral group of order 16.

1. Inverses

A general symmetry can be written in the form

$$\begin{aligned}\mathcal{T}^s \mathcal{R}^a \mathcal{S}^m &= \mathcal{T}^s \chi^a \mathcal{Y}^a \mathcal{C}^m \mathcal{U}^m \chi^m \\ &= \mathcal{T}^s \mathcal{U}^{(-1)^a m} \mathcal{Y}^a \chi^{a+m} \mathcal{C}^m,\end{aligned}\tag{A3}$$

for $a \in \{0, 1\}$, $m \in \{0, \dots, 7\}$ and $s \in [0, 2\pi)$. When $a = 0$, this has inverse

$$\begin{aligned}(\mathcal{T}^s \mathcal{R}^0 \mathcal{S}^m)^{-1} &= \mathcal{S}^{-m} \mathcal{T}^{-s} \\ &= \mathcal{C}^{-m} \mathcal{U}^{-m} \chi^{-m} \mathcal{T}^{-s} \\ &= \mathcal{T}^{-(-1)^{-m} s} \mathcal{U}^{-m} \chi^{-m} \mathcal{C}^{-m} \\ &= \mathcal{T}^{(-1)^{1+m} s} \mathcal{R}^0 \mathcal{S}^{-m},\end{aligned}\tag{A4}$$

and for $a = 1$,

$$\begin{aligned}(\mathcal{T}^s \mathcal{R}^1 \mathcal{S}^m)^{-1} &= \mathcal{S}^{-m} \mathcal{R} \mathcal{T}^{-s} \\ &= \mathcal{C}^{-m} \mathcal{U}^{-m} \chi^{1-m} \mathcal{Y} \mathcal{T}^{-s} \\ &= \mathcal{T}^{-(-1)^{1-m} s} \mathcal{U}^{-m} \mathcal{Y}^1 \chi^{1+m} \mathcal{C}^m \\ &= \mathcal{T}^{(-1)^m s} \mathcal{R}^1 \mathcal{S}^m,\end{aligned}\tag{A5}$$

with the exponents of \mathcal{T} and \mathcal{S} being understood modulo 2π and 8 respectively.

2. Equivalent solutions

Suppose we have an initial condition ω_0 giving rise to an RPO relative to $\mathcal{T}^s \mathcal{R}^a \mathcal{S}^m$, i.e.

$$\omega_T = \mathcal{T}^s \mathcal{R}^a \mathcal{S}^m \omega_0.\tag{A6}$$

Then

$$\mathcal{R} \omega_T = \mathcal{R} \mathcal{T}^s \mathcal{R}^a \mathcal{S}^m \omega_0 = \mathcal{T}^{-s} \mathcal{R}^a \mathcal{S}^{-m} (\mathcal{R} \omega_0),\tag{A7}$$

which means that any RPOs with $m = 5, 6, 7$ are equivalent to ones with $m = 3, 2, 1$ respectively, after rotating the vorticity field by π . Furthermore,

$$\mathcal{S} \omega_T = \mathcal{S} \mathcal{T}^s \mathcal{R}^a \mathcal{S}^m \omega_0 = \begin{cases} \mathcal{T}^s \mathcal{R}^a \mathcal{S}^m (\mathcal{S} \omega_0), & a = 0, \\ \mathcal{T}^s \mathcal{R}^a \mathcal{S}^{m-2} (\mathcal{S} \omega_0), & a = 1, \end{cases}\tag{A8}$$

so the classes with $a = 1$ and m even are all equivalent, likewise for $a = 1$ and m odd. If $a = 1$ and m is even, we have

$$\mathcal{T}^{-s/2} \omega_T = \mathcal{T}^{s/2} \mathcal{R}^a \mathcal{S}^m \omega_0 = \mathcal{R}^a \mathcal{S}^m (\mathcal{T}^{-s/2} \omega_0)\tag{A9}$$

so the orbit is equivalent to one with $s = 0$. If $a = 0$ and m is odd, the same result holds.

Therefore, it is sufficient to consider only the following cases:

- $a = 0, m = 0$ with $s \in [0, 2\pi)$,
- $a = 0, m = 1$ with $s = 0$,
- $a = 0, m = 2$ with $s \in [0, 2\pi)$,
- $a = 0, m = 3$ with $s = 0$,
- $a = 0, m = 4$ with $s \in [0, 2\pi)$,
- $a = 1, m = 0$ with $s = 0$,
- $a = 1, m = 1$ with $s \in [0, 2\pi)$.

In fact, it is not necessary to consider the full range of s in these cases, but we do not make this reduction.

-
- [1] B. Eckhardt and G. Ott, Periodic orbit analysis of the Lorenz attractor, *Zeitschrift für Physik B Condensed Matter* **93**, 259 (1994).
 - [2] D. Viswanath, Symbolic dynamics and periodic orbits of the Lorenz attractor, *Nonlinearity* **16**, 1035 (2003).
 - [3] P. Cvitanović, R. Artuso, R. Mainieri, G. Tanner, and G. Vattay, *Chaos: Classical and Quantum* (Niels Bohr Inst., Copenhagen, 2016).
 - [4] J. Page and R. R. Kerswell, Searching turbulence for periodic orbits with dynamic mode decomposition, *Journal of Fluid Mechanics* **886**, A28 (2020).
 - [5] G. J. Chandler and R. R. Kerswell, Invariant recurrent solutions embedded in a turbulent two-dimensional Kolmogorov flow, *Journal of Fluid Mechanics* **722**, 554 (2013).
 - [6] E. M. Redfern, A. L. Lazer, and D. Lucas, Dynamically relevant recurrent flows obtained via a nonlinear recurrence function from two-dimensional turbulence, *Physical Review Fluids* **9**, 124401 (2024).
 - [7] J. Page, P. Norgaard, M. P. Brenner, and R. R. Kerswell, Recurrent flow patterns as a basis for two-dimensional turbulence: Predicting statistics from structures, *Proceedings of the National Academy of Sciences* **121**, e2320007121 (2024).
 - [8] J. Page, J. Holey, M. P. Brenner, and R. R. Kerswell, Exact coherent structures in two-dimensional turbulence identified with convolutional autoencoders, *Journal of Fluid Mechanics* **991**, A10 (2024).
 - [9] J. P. Parker and T. M. Schneider, Variational methods for finding periodic orbits in the incompressible Navier–Stokes equations, *Journal of Fluid Mechanics* **941**, A17 (2022).
 - [10] P. Beck, J. P. Parker, and T. M. Schneider, Data-driven guessing and gluing of unstable periodic orbits, *Physical Review E* **112**, 024203 (2025).
 - [11] B. Kaszás and G. Haller, Joint reduced model for the laminar and chaotic attractors in plane Couette flow, *Journal of Fluid Mechanics* **1023**, 10.1017/jfm.2025.10795 (2025).
 - [12] T. Cohen and M. Welling, Group equivariant convolutional networks, in *International conference on machine learning* (PMLR, 2016) pp. 2990–2999.
 - [13] E. Hoogeboom, V. G. Satorras, C. Vignac, and M. Welling, Equivariant diffusion for molecule generation in 3d, in *International conference on machine learning* (PMLR, 2022) pp. 8867–8887.
 - [14] O. Vega, J. Komijani, A. El-Khadra, and M. Marinkovic, Group-Equivariant Diffusion Models for Lattice Field Theory, arXiv preprint arXiv:2510.26081 (2025).
 - [15] C. Liu, S. Vadgama, D. Ruhe, E. Bekkers, and P. Forré, Clifford Group Equivariant Diffusion Models for 3D Molecular Generation, arXiv preprint arXiv:2504.15773 (2025).
 - [16] M. Raissi, P. Perdikaris, and G. E. Karniadakis, Physics-informed neural networks: A deep learning framework for solving forward and inverse problems involving nonlinear partial differential equations, *Journal of Computational physics* **378**, 686 (2019).
 - [17] L. Yang, D. Zhang, and G. E. Karniadakis, Physics-informed generative adversarial networks for stochastic differential equations, *SIAM Journal on Scientific Computing* **42**, A292 (2020).
 - [18] K. Ciftci and K. Hackl, A physics-informed GAN framework based on model-free data-driven computational mechanics, *Computer Methods in Applied Mechanics and Engineering* **424**, 116907 (2024).
 - [19] N. Platt, L. Sirovich, and N. Fitzmaurice, An investigation of chaotic Kolmogorov flows, *Physics of Fluids A: Fluid Dynamics* **3**, 681 (1991).
 - [20] M. Farazmand and T. P. Sapsis, A variational approach to probing extreme events in turbulent dynamical systems, *Science advances* **3**, e1701533 (2017).
 - [21] D. Lucas and T. Yasuda, Stabilization of exact coherent structures in two-dimensional turbulence using time-delayed feedback, *Physical Review Fluids* **7**, 014401 (2022).
 - [22] C. E. P. De Jesús and M. D. Graham, Data-driven low-dimensional dynamic model of Kolmogorov flow, *Physical Review Fluids* **8**, 044402 (2023).
 - [23] A. Racca, N. A. K. Doan, and L. Magri, Predicting turbulent dynamics with the convolutional autoencoder echo state network, *Journal of Fluid Mechanics* **975**, A2 (2023).
 - [24] B. Suri, J. Tithof, R. Mitchell, R. O. Grigoriev, and M. F. Schatz, Velocity profile in a two-layer Kolmogorov-like flow, *Physics of Fluids* **26** (2014).
 - [25] B. Suri, J. Tithof, R. O. Grigoriev, and M. F. Schatz, Unstable equilibria and invariant manifolds in quasi-two-dimensional Kolmogorov-like flow, *Physical Review E* **98**, 023105 (2018).
 - [26] A. Cleary and J. Page, Characterizing the Reynolds number dependence of the chaotic attractor in two-dimensional turbulence with dimension-minimizing autoencoders, *Physical Review E* **112**, 055105 (2025).
 - [27] A. Cleary and J. Page, Dynamical relevance of periodic orbits under increasing Reynolds number and connections to inviscid dynamics, arXiv preprint arXiv:2502.06475 (2025).
 - [28] P. Cvitanović, R. L. Davidchack, and E. Siminos, On the state space geometry of the Kuramoto–Sivashinsky flow in a periodic domain, *SIAM Journal on Applied Dynamical Systems* **9**, 1 (2010).
 - [29] S. Azimi, O. Ashtari, and T. M. Schneider, Constructing periodic orbits of high-dimensional chaotic systems by an adjoint-based variational method, *Physical Review E* **105**, 014217 (2022).

- [30] P. Cvitanović, Dynamical averaging in terms of periodic orbits, *Physica D: Nonlinear Phenomena* **83**, 109 (1995).
- [31] Y. Lan, Cycle expansions: From maps to turbulence, *Communications in Nonlinear Science and Numerical Simulation* **15**, 502 (2010).
- [32] N. B. Budanur, D. Borrero-Echeverry, and P. Cvitanović, Periodic orbit analysis of a system with continuous symmetry—A tutorial, *Chaos: An Interdisciplinary Journal of Nonlinear Science* **25** (2015).
- [33] D. Wilczak and P. Zgliczyński, A geometric method for infinite-dimensional chaos: Symbolic dynamics for the Kuramoto-Sivashinsky PDE on the line, *Journal of Differential Equations* **269**, 8509 (2020).
- [34] M. Abadie, P. Beck, J. P. Parker, and T. M. Schneider, The topology of a chaotic attractor in the Kuramoto–Sivashinsky equation, *Chaos: An Interdisciplinary Journal of Nonlinear Science* **35** (2025).
- [35] D. Wilczak, Abundance of heteroclinic and homoclinic orbits for the hyperchaotic rössler system, *Discrete Contin. Dyn. Syst. Ser. B* **11**, 1039 (2009).
- [36] L. Van Veen, S. Kida, and G. Kawahara, Periodic motion representing isotropic turbulence, *Fluid dynamics research* **38**, 19 (2006).
- [37] I. Goodfellow, J. Pouget-Abadie, M. Mirza, B. Xu, D. Warde-Farley, S. Ozair, A. Courville, and Y. Bengio, Generative adversarial nets, *Advances in neural information processing systems* **27** (2014).
- [38] D. P. Kingma, Auto-encoding variational Bayes, arXiv preprint arXiv:1312.6114 (2013).
- [39] J. Sohl-Dickstein, E. Weiss, N. Maheswaranathan, and S. Ganguli, Deep unsupervised learning using nonequilibrium thermodynamics, in *International conference on machine learning* (PMLR, 2015) pp. 2256–2265.
- [40] J. Ho, A. Jain, and P. Abbeel, Denoising diffusion probabilistic models, *Advances in neural information processing systems* **33**, 6840 (2020).
- [41] J. Song, C. Meng, and S. Ermon, Denoising diffusion implicit models, arXiv preprint arXiv:2010.02502 (2020).
- [42] J. Page, M. P. Brenner, and R. R. Kerswell, Revealing the state space of turbulence using machine learning, *Physical Review Fluids* **6**, 034402 (2021).
- [43] O. Ronneberger, P. Fischer, and T. Brox, U-net: Convolutional networks for biomedical image segmentation, in *International Conference on Medical image computing and computer-assisted intervention* (Springer, 2015) pp. 234–241.
- [44] A. Vaswani, N. Shazeer, N. Parmar, J. Uszkoreit, L. Jones, A. N. Gomez, L. Kaiser, and I. Polosukhin, Attention is all you need, *Advances in neural information processing systems* **30** (2017).
- [45] M. Sipper, Neural networks with à la carte selection of activation functions, *SN Computer Science* **2**, 470 (2021).
- [46] D. Viswanath, The Lindstedt–Poincaré technique as an algorithm for computing periodic orbits, *SIAM review* **43**, 478 (2001).
- [47] Y. Lan and P. Cvitanović, Variational method for finding periodic orbits in a general flow, *Physical Review E* **69**, 016217 (2004).
- [48] J. P. Parker, O. Ashtari, and T. M. Schneider, Predicting chaotic statistics with unstable invariant tori, *Chaos: An Interdisciplinary Journal of Nonlinear Science* **33** (2023).
- [49] D. Viswanath, Recurrent motions within plane Couette turbulence, *Journal of Fluid Mechanics* **580**, 339 (2007).
- [50] J. P. Parker and T. M. Schneider, Invariant tori in dissipative hyperchaos, *Chaos: An Interdisciplinary Journal of Nonlinear Science* **32**, 113102 (2022).